Journal of Alloys and Compounds 897 (2022) 163158

Contents lists available at ScienceDirect

Journal of Alloys and Compounds

journal homepage: www.elsevier.com/locate/jalcom

Spinel $CoMn_2O_4$ hollow nanospheres for very wide linear and sensitive detection of hydrogen peroxide

Yuan Gao[a], De-Rui Kong[a], Zhu-Yan Zhang[b], Xian-Fa Zhang[a], Zhao-Peng Deng[a,*], Li-Hua Huo[a], Shan Gao[a,*]

[a] Key Laboratory of Functional Inorganic Material Chemistry, Ministry of Education, School of Chemistry and Materials Science, Heilongjiang University, Harbin 150080, People's Republic of China
[b] College of Pharmacy, Harbin Medical University, Harbin 150081, People's Republic of China

ARTICLE INFO

Article history:
Received 27 August 2021
Received in revised form 22 November 2021
Accepted 6 December 2021
Available online 8 December 2021

Keywords:
Spinel oxides
$CoMn_2O_4$
Electrochemical sensor
H_2O_2
Hollow nanosphere

ABSTRACT

Spinel $CoMn_2O_4$ hollow nanospheres with diameter of ~200 nm were facilely prepared using polyvinylpyrrolidone (PVP) as structure directing agent, which possessed hierarchical pore distribution and large surface area of 43.5 $m^2 g^{-1}$. The above nanomaterials were simply drop-coated on the surface of bare glass carbon electrode (GCE) to generate $CoMn_2O_4$/GCE. In phosphate buffer (PBS, pH = 7), the modified electrode presents rapidly sensitive response and low detection limit (0.38 μM) to H_2O_2. Especially, its linear detection range (0.0012–100.4 mM) is the widest among reported spinel oxide-based electrochemical sensors to date. This excellent electrocatalytic H_2O_2 sensing performance primarily derives from the synergism of unique hollow nanosphere structure and the redox coupling of Co^{3+}/Co^{2+} and Mn^{3+}/Mn^{2+}. In addition, the $CoMn_2O_4$/GCE sensor also shows good H_2O_2 recovery in rat serum and commercial disinfectant, indicating that it has a certain potential application in related environmental and biological fields.

1. Introduction

Hydrogen peroxide (H_2O_2) with good redox and microbial control properties has been widely used in food processing, clinical medicine, and environmental testing. Especially, as a general-purpose green oxidant, it is often used as food antiseptic additives in milk and beverages, as well as disinfectants in household detergent and contact lens care solutions. However, excessive use or intake of H_2O_2 can pose serious risks to human health and environmental safety [1,2]. Therefore, it is of great practical significance to quickly and accurately detect H_2O_2 in real time. Very recently, in contrast to single transition metal oxides, nanostructured spinel-type AB_2O_4 bimetallic oxides have been considered as promising electrocatalysts for H_2O_2 detection with high response and good stability owing to their excellent conductivity and catalytic activity [3–5]. Nevertheless, their very narrow range of linear detection concentrations reported so far still needs to be widened, which can reduce the complex process of sample preparation and the detection period of electrochemical analysis, and also facilitate portable operation in some practical applications [6,7]. Thus, it is necessary to develop an electrochemical sensor based on spinel oxides with wide linear detection and high sensitivity to H_2O_2.

$CoMn_2O_4$ is known to be an important spinel-type manganese-based electrocatalytic material, which may be related to the superior potential and fast electronic transport characteristics of cobalt and manganese ions. Some recent reports have illustrated that synergism of the two metal cations can effectively reduce the activation energy of charge transfer between them, and the existence of Co^{3+}/Co^{2+} and Mn^{3+}/Mn^{2+} redox coupling also improves the catalytic active site of electrode materials [8,9]. Hence, $CoMn_2O_4$-based electrocatalysts have attracted great interest and shown excellent competitiveness in electrochemical analysis. For example, $CoMn_2O_4$/rGO composite modified nickel foam electrode reported in 2021 presented good electrochemical sensing performance to glucose [10]. $CoMn_2O_4$ microspheres/GCE fabricated in 2020 showed highly sensitive response to Rizatriptan benzoate [11]. Simultaneously, $CoMn_2O_4$-based electrochemical sensors still presented good detection capabilities towards heavy metal ions (Pb^{2+}, Cd^{2+} and Hg^{2+}) [12–15]. However, there has been only one report concerning on its application as electrochemical H_2O_2 sensor to date. In 2018, Liu et al. assembled a novel self-powered bio-electrochemical sensor with bio-anode and $CoMn_2O_4$/graphite cathode, which presented good electrochemical response to H_2O_2 with linear detection range of mM-level concentrations [16]. It should be pointed out that

* Corresponding authors.
E-mail addresses: dengzhaopeng@hlju.edu.cn (Z.-P. Deng), shangao67@yahoo.com (S. Gao).

https://doi.org/10.1016/j.jallcom.2021.163158
0925-8388/

electrochemically active bacteria needed more than three months of culture to obtain a stable electrical signal output before the above sensor being actually used, which is not conducive to simple, fast and real-time monitoring. Meanwhile, the high detection limit (40.2 μM) and narrow linear range still needed to be further improved.

The sensing performance of enzyme-free electrochemical sensors largely depends on the microstructure of electrocatalytic materials, such as morphology, particle size, pore structure and specific surface area [17,18]. The hollow nanospheres assembled from small-size particles have rich mesoporous structure and large specific surface area, which is beneficial to increase the mass transfer efficiency and expose more electrochemical active sites. At the same time, the synergistic effect of mixed valence cobalt and manganese ions can significantly improve the conductivity and electrochemical sensing performance of $CoMn_2O_4$ sensors [11], further helping to broaden the linear detection range of H_2O_2 in combination with hollow nanosphere structure. In view of these points, $CoMn_2O_4$ hollow nanospheres with diameter of ~200 nm were facilely prepared with PVP as structure directing agent, which were then drop-coating onto bare GCE surface. The $CoMn_2O_4$/GCE modified electrode shows rapidly sensitive response and low detection limit of 0.38 μM to H_2O_2 in PBS medium. In particular, its linear detection range (0.0012–100.4 mM) is the widest among reported spinel oxide electrochemical sensors. Meanwhile, the modified electrode has a good recovery rate for H_2O_2 in rat serum and commercially available disinfectant, indicating its potential practical applications in relevant environmental, food and biological fields.

2. Experimental

2.1. Chemical reagents

The reagents of $Mn(Ac)_2{\cdot}4H_2O$, $Co(Ac)_2{\cdot}H_2O$, KOH, ethylene glycol (EG), nafion, Na_2HPO_4, NaH_2PO_4, glucose (Glu), dopamine (DA), uric acid (UA), ascorbic acid (AA), epinephrine (E), glutamic acid (Gln), L-cysteine (Lcy), sodium nitrite ($NaNO_2$), sodium chloride (NaCl) and 30 wt% H_2O_2, were analytically pure and directly utilized. The rat serums were provided by Harbin Medical University, China, and the disinfectant (containing 3% H_2O_2) were purchased from local supermarket. The instruments for the characterization of materials were all presented in Supplementary material.

2.2. Preparation of mesoporous $CoMn_2O_4$ hollow nanospheres

The synthesis process of spinel $CoMn_2O_4$ hollow nanospheres is shown in Scheme 1. PVP (0.11 g), $Co(Ac)_2{\cdot}4H_2O$ (1 mmol) and $Mn(Ac)_2{\cdot}4H_2O$ (2 mmol) were added in 60 mL ethylene glycol (EG) in turn to generate transparent solution. Subsequently, the obtained solution was transferred into a round bottom flask with reflux for 120 min in oil bath at 170 °C. After cooling to room temperature, light purple precipitations (precursor) were isolated through centrifugation and cleaned twice using ethanol followed by drying at 60 °C. Ultimately, the precursor was calcined at 600 °C in air for 2 h (heating rate: 1 °C min^{-1}) to obtain dark green powder. Moreover, similar synthesis method was used to prepare Co_3O_4 and Mn_2O_3 control samples.

2.3. Preparation of modified electrodes

At the beginning, 4.0 mg $CoMn_2O_4$ samples were dispersed into 0.5 wt% nafion-ethanol solution (1 mL) to form a uniform suspension. Before modifying the bare GCE, its surface (5 mm in diameter) was polished by Al_2O_3 with particle size of 0.05 μm, and then ultrasonic cleaning was performed in dilute HNO_3 (1:1), ethanol and distilled water solutions. Finally, the above-mentioned suspension (10 μL) was evenly drop-coating onto the clean GCE surface followed by drying at room temperature to obtain the $CoMn_2O_4$/GCE modified electrode. Additionally, the Mn_2O_3/GCE and Co_3O_4/GCE modified electrodes were also prepared in a similar manner.

2.4. Electrochemical tests

The electrochemical tests were carried out at CHI-760E workstation (Shanghai Chenhua Instrument Co., Ltd., China) using three-electrode system with the modified GCE, saturated Ag/AgCl and platinum mesh as the working, reference and auxiliary electrodes, respectively. Electrochemical impedance experiments were conducted in 5 mmol L^{-1} $[Fe(CN)_6]^{3-/4-}$ (1:1) containing 0.1 mol L^{-1} KCl with a frequency range of 10^{-2}–10^5 Hz and an amplitude of 5 mV. The apparent activity area of the modified electrode was determined by chronocoulometry in 0.1 mmol L^{-1} $[Fe(CN)_6]^{3-/4-}$ solution containing 2.0 mol L^{-1} KCl. Electrochemical tests of different concentrations of H_2O_2 were performed in 0.05 mol L^{-1} phosphate buffer (PBS, pH = 7.0) using cyclic voltammetry. The electrocatalytic H_2O_2 reduction was tested by amperometric method in the above PBS. Before these electrochemical experiments at room temperature, the electrolyte was purged with high-purity nitrogen to remove dissolved oxygen and maintain the nitrogen atmosphere during the test.

2.5. Preparation of real samples

Rat serum sample and commercial disinfectant were treated in advance before electrochemical test. The rat serum sample was centrifuged at 4000 rpm for 5 min, and the supernatant (serum) was collected and diluted to 100 times by the addition of PBS to form a 1% serum solution. Furthermore, the commercial disinfectant was also diluted by 10 times with PBS.

3. Results and discussion

3.1. Material characterization

The IR spectrum of precursor in Fig. 1A shows a broad absorption peak at 3337 cm^{-1} that can be attributed to the stretching vibration of O-H in absorption water. The absorption peaks at 2920 and

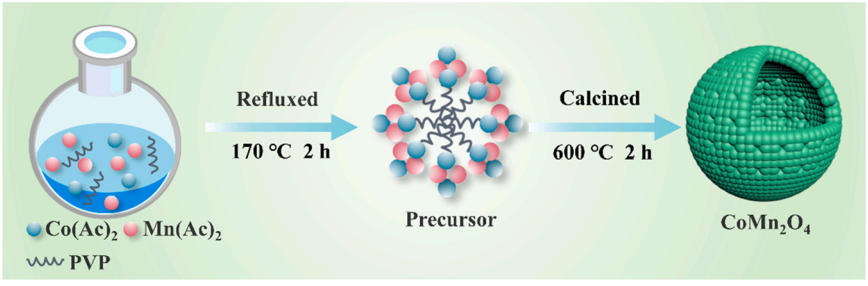

Scheme 1. Synthetic diagram of spinel $CoMn_2O_4$ hollow nanospheres.

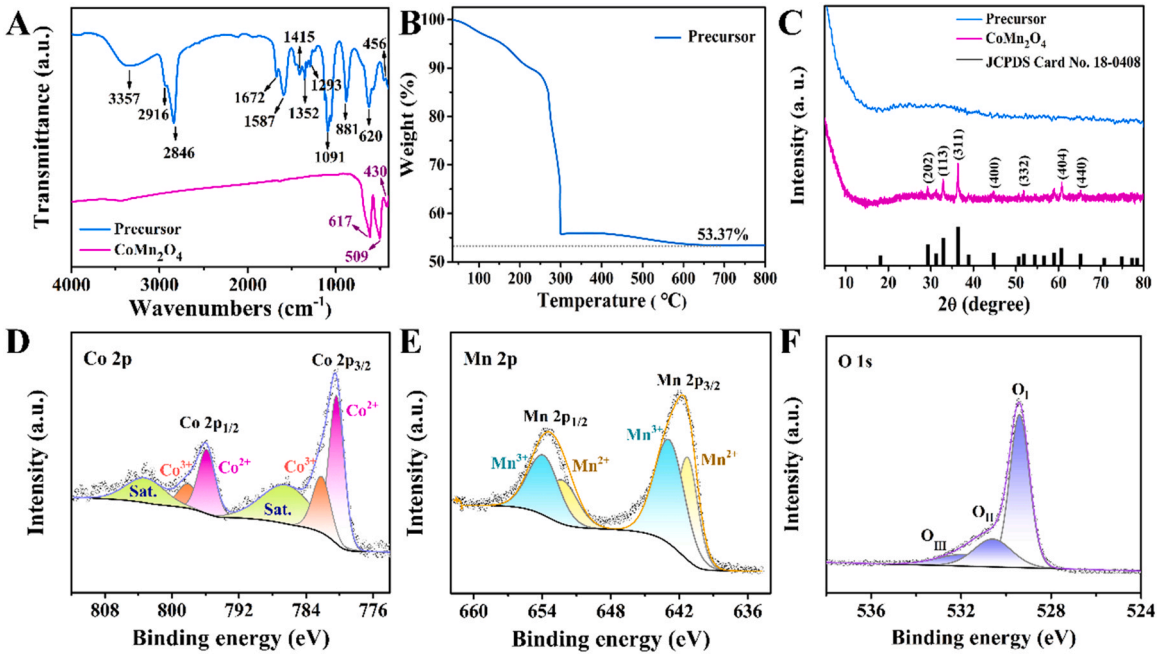

Fig. 1. (A) IR spectra of precursor and calcined product; (B) TG curve of precursor in air atmosphere; (C) PXRD patterns of precursor and calcined product; High-resolution XPS spectra of $CoMn_2O_4$ product: Co 2p (D), Mn 2p (E) and O 1s (F).

2846 cm^{-1} can refer to the stretching vibrations of C-H in -CH_3 and -CH_2- groups. The peaks at 1672 and 1293 cm^{-1} are assigned to the C═O and C-N stretching vibrations of PVP molecules [19], while the absorption peaks at 1587, 1352 and 1091 cm^{-1} are the stretching vibrations of $\nu_{as}(CO_2^-)$, $\nu_s(CO_2^-)$ and ν(C-O), respectively. The characteristic vibrations of Mn—O and Co—O coordination bonds appear at 456 and 620 cm^{-1} [20]. Accordingly, the as-synthesized precursor may be Co/Mn acetate containing a small amount of PVP and EG. The TG curve of precursor in air atmosphere is shown in Fig. 1B, in which the continuous weight loss appears prior to 600 °C, being ascribed to the loss of adsorbed water, decomposition of PVP, EG and acetate, as well as the formation of metal oxide nanocrystals. The final residual amount remains 53.37%. Therefore, the precursor was calcined in air at 600 °C for 2 h to obtain dark green product. It can be seen from the IR spectrum of calcined product (Fig. 1A) that the characteristic vibration peaks of organic groups in precursor disappear, indicating the complete removal of PVP, EG and acetate. The two strong absorption peaks at 617 and 509 cm^{-1} represent the characteristic vibrations of octahedral Mn-O and tetrahedral Co—O bonds [21], while the peak at 430 cm^{-1} can be referred to the characteristic vibration of Co—O—Mn bond, indicating the formation of spinel $CoMn_2O_4$ after calcination [22].

XRD characterization was performed in order to determine the crystal phase of precursor and calcined product. As shown in Fig. 1C, almost no diffraction peaks are observed in the XRD pattern of precursor, indicating its amorphous state. After the precursor being calcined in air at 600 °C, its XRD pattern shows clear diffraction peaks, all of which fully correspond to the crystal planes of standard card (JCPDS No. 18-0408) of tetragonal $CoMn_2O_4$ spinel structure. It should be noted that weak diffraction peaks indicate the small particle size of nanomaterial and no other additional peaks are observed, demonstrating the formation of pure $CoMn_2O_4$ nanomaterial after the precursor being calcined in air at 600 °C. In addition, the XRD patterns of the two control samples synthesized by the same method are shown in Fig. S1. All of their diffraction peaks separately correspond to the crystal planes of Mn_2O_3 (JCPDS No. 24-0508) and Co_3O_4 (JCPDS No. 43-1003), indicating that the as-synthesized control samples are pure Mn_2O_3 and Co_3O_4 materials.

The full XPS spectrum of calcined product in Fig. S2 shows that only Co, Mn and O elements are observed with the atomic ratio of Co/Mn being 1:2. This result further proves that the calcined product at 600 °C is spinel $CoMn_2O_4$. Fig. 1D is the high-resolution Co 2p XPS spectrum, in which the binding energies of 795.9 and 780.3 eV can be attributed to Co $2p_{1/2}$ and Co $2p_{3/2}$ of Co^{2+} ion, while the binding energies of 798.1 and 782.2 eV refer to Co $2p_{1/2}$ and Co $2p_{3/2}$ of Co^{3+} ion. The integral area ratio of Co^{3+}/Co^{2+} is 0.31:0.69, indicating that the Co ions exist in mixed valence state of Co^{3+} and Co^{2+} [23]. In Fig. 1E, the binding energy peaks at 653.9 and 642.9 eV are assigned to the Mn $2p_{1/2}$ and Mn $2p_{3/2}$ of Mn^{3+} ion, while the peaks at 652.4 and 641.3 eV can refer to Mn $2p_{1/2}$ and Mn $2p_{3/2}$ of Mn^{2+} ion. The integral area ratio of Mn^{3+}/Mn^{2+} is 0.59:0.41, which indicates that Mn ions also exist in the form of mixed Mn^{2+} and Mn^{3+} [24]. Therefore, spinel $CoMn_2O_4$ hollow nanospheres have inherent Co^{3+}/Co^{2+} and Mn^{3+}/Mn^{2+} redox coupling, and the synergism of Co and Mn ions in different valence states can increase the conductivity and catalytic activity of electrode materials, thereby effectively enhancing the electrocatalytic properties of $CoMn_2O_4$ hollow nanospheres. Fig. 1F is the high-resolution O 1s XPS spectrum, in which the binding energy peaks at 529.4, 530.6 and 531.9 eV correspond to the metal-oxygen bond (O_I), surface adsorbed oxygen (O_{II}) and surface adsorbed water (O_{III}) in the $CoMn_2O_4$ hollow nanospheres, respectively [16].

The SEM image of amorphous precursor in Fig. 2A shows the morphology of nanospheres with good dispersion, which has smooth surface and average particle diameter of 200–300 nm. It can be seen from Fig. 2B that the calcined product better retains the nanosphere morphology of precursor. In comparison, the surface becomes rough and the average particle diameter reduces to ~200 nm. The obvious change of morphology may be originated from the decomposition of residual organic matters in precursor during the calcination process, resulting in the cross-linkage of nanoparticles and the shrinkage of microstructure. To further observe the fine structure of nanospheres, we carried out TEM characterization. As can be seen from the TEM image in Fig. 2C, the morphology of $CoMn_2O_4$ material is hollow nanosphere structure with particle size of ~200 nm. The shell of nanosphere is cross-linked by small-size nanoparticles, which also generate abundant pores on its surface.

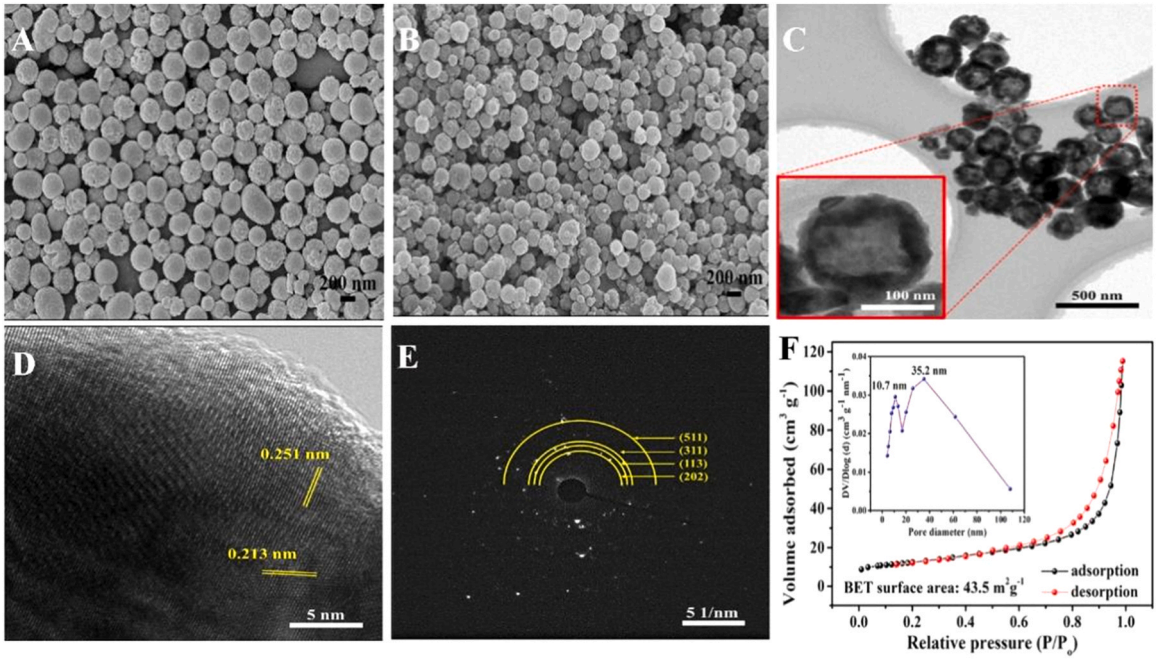

Fig. 2. SEM images of precursor (A) and calcined product (B); TEM (C), HRTEM (D), SAED (E) and N_2 adsorption-desorption isotherm (F) of $CoMn_2O_4$ nanomaterial (inset: pore size distribution).

Such hollow structure is conductive to increase mass transfer efficiency and accommodate more target analytes, which in turn broadens the linear detection range of electrode materials [25]. The HRTEM image (Fig. 2D) clearly shows the lattice fringe spacing of 0.251 and 0.213 nm, which correspond to the *d*-values of (311) and (440) planes in tetragonal $CoMn_2O_4$ spinel. The diffraction rings in the selected area electron diffraction (SAED, Fig. 2E) pattern correspond to the (511), (311), (113) and (202) planes of polymorphic $CoMn_2O_4$. In addition, the N_2 adsorption-desorption curve (Fig. 2F) of $CoMn_2O_4$ nanomaterial belongs to type IV isotherms accompanied by an obvious H3 hysteresis loop, indicating the existence of hierarchical pores originating from cross-linkage of nanoparticles and pyrolysis of organic components [26]. The pore size distribution mainly concentrates at 10.7 and 35.2 nm, and the specific surface area is as large as 43.5 $m^2\ g^{-1}$. This hierarchical pore structure is in favor of the rapid analytes diffusion and charges transfer, and the large specific surface area can expose more active sites and promote the contact probability between target molecule and electrocatalyst. Meanwhile, Co^{3+}/Co^{2+} and Mn^{3+}/Mn^{2+} redox coupling can effectively improve the conductivity and catalytic efficiency of electrode materials [27]. Therefore, it could be predicted that the porous $CoMn_2O_4$ hollow nanospheres should have good electrocatalytic H_2O_2 sensing performance.

3.2. Electrochemical properties of modified electrodes

Electrochemical impedance spectrum (EIS) is often used to monitor the electron transfer and surface resistance change of modified electrodes [28]. Fig. 3A shows the Nyquist plots of different modified electrodes in 5 mM $[Fe(CN)_6]^{3-/4-}$ containing 0.1 M KCl and the inset is the Randles equivalent circuit model. The semicircle diameter of high frequency region reflects the value of charge transfer resistance R_{ct}. Large semicircle diameter indicates high R_{ct} value and low electron transfer efficiency of modified electrodes [29]. It can be seen from Fig. 3A that bare GCE (curve a) shows the lowest R_{ct}, indicating the fastest electron transfer rate between bare GCE and $[Fe(CN)_6]^{3-/4-}$ probe. When the three metal oxides were modified onto bare GCE surface, the semicircle diameter of high frequency region gradually increases in the order of $CoMn_2O_4$/GCE < Mn_2O_3/GCE < Co_3O_4/GCE. The increased R_{ct} demonstrates the successful assembly of the above modified electrodes. In contrast to the large R_{ct} values of Mn_2O_3/GCE (curve b, 1070 Ω) and Co_3O_4/GCE (curve c, 2327 Ω), the relatively small R_{ct} value of 920 Ω for $CoMn_2O_4$/GCE (curve d) indicates its good electrical conductivity, which can facilitate the rapid electron transfer between $[Fe(CN)_6]^{3-}$/$[Fe(CN)_6]^{4-}$ and electrode. The cyclic voltammetry (CV) curves of different modified electrodes are illustrated in Fig. 3B, in which the

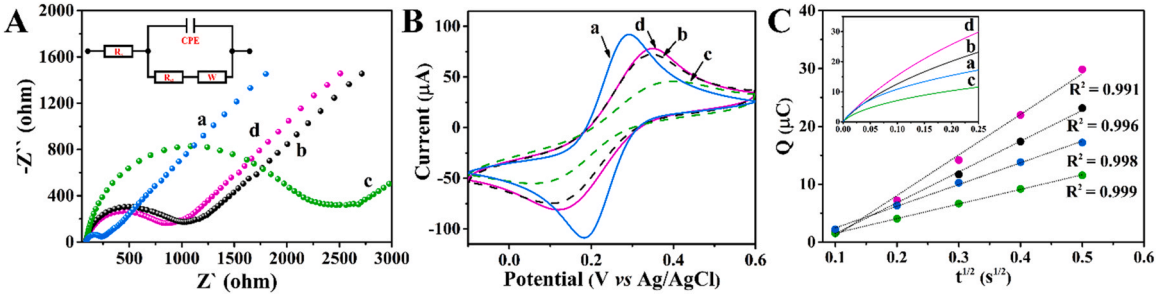

Fig. 3. EIS (A), CV curves (B) and Q-$t^{1/2}$ plots (C) of bare GCE and modified electrodes [inset in A: equivalent circuit diagram; inset in C: the Q-t curves of GCE (a), Mn_2O_3/GCE (b), Co_3O_4/GCE (c), $CoMn_2O_4$/GCE (d)].

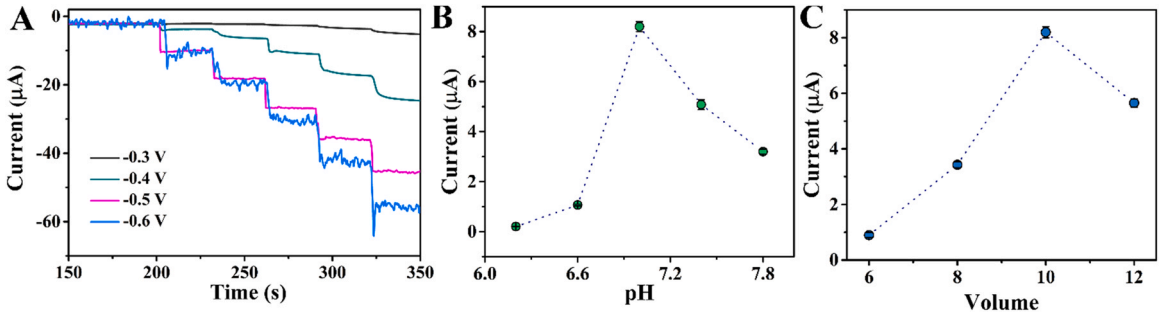

Fig. 4. (A) Current responses under different negative working potentials; (B) pH-dependent current intensity change; (C) Volume-dependent current intensity change.

peak current of $CoMn_2O_4$/GCE is higher than those of Co_3O_4/GCE and Mn_2O_3/GCE, further proving that $CoMn_2O_4$ hollow nanospheres have better charge conductivity than single metal oxides (Co_3O_4, Mn_2O_3). These results are consistent with the above EIS analyses.

The *Q-t* curves (inset in Fig. 3C) of bare GCE and modified electrodes were tested with chronocoulometry. The apparent electrode area (*A*) of different electrodes is calculated by combining with Anson's equation [30]:

$$Q(t) = \frac{2nFAcD^{1/2}t^{1/2}}{\pi^{1/2}} + Q_{dl} + Q_{ads} \quad (1)$$

Among them, *n* is the number of transferred electrons, *A* is the apparent electrode area, *c* is the concentration of $[Fe(CN)_6]^{3-/4-}$ solution, *F* is the Faraday constant, *D* is the diffusion coefficient (7.6×10^{-6} cm^2 s^{-1}) [31], Q_{dl} is a double-layer charge, and Q_{ads} is a Faradic charge. As illustrated in Fig. 3C, the $Q\text{-}t^{1/2}$ curves of the four electrodes have good linear relationships, and the slopes of four fitted lines (a, b, c, d) are 37.5, 53.26, 25.2 and 70.1 μC $s^{-1/2}$, respectively. According to Eq. (1), the calculated values of *A* for bare GCE, Co_3O_4/GCE, Mn_2O_3/GCE and $CoMn_2O_4$/GCE electrodes are separately 0.125, 0.084, 0.177 and 0.233 cm^2, indicating that the modified $CoMn_2O_4$/GCE has the largest apparent electrode area *A*, which may be related to the large specific surface area of $CoMn_2O_4$ hollow nanospheres. The large *A* value increases the reaction active sites on the electrode surface and the adsorption sites of target analytes, but also provides a more effective platform for electrolyte penetration and electron migration, thereby enhancing the electrochemical sensing properties of $CoMn_2O_4$ nanomaterial to H_2O_2.

3.3. Electrocatalytic behavior of modified electrodes towards H_2O_2

Amperometric method is often used as a technique for estimating the sensing properties of electrochemical sensors. For the sake of studying the electrocatalytic H_2O_2 properties of $CoMn_2O_4$/GCE, we firstly optimized the electrochemical experimental conditions. The current–time curves of $CoMn_2O_4$/GCE at different negative operating potentials with continuous addition of 5 mM H_2O_2 in 0.05 M PBS (pH = 7.0) were tested by amperometric method. As shown in Fig. 4A, as the negative working potential changes from −0.3 V to −0.6 V, the change in current response (ΔI) of modified electrode gradually increases. Meanwhile, the corresponding resistance also shows a decreasing trend with the increment of negative working potential from −0.3 to −0.6 V (Fig. S3), which is consistent with the current change (ΔI), thereby verifying the relationship between negative operating potential and current/resistance. Furthermore, considering the significantly larger current signal noise at −0.6 V, we select −0.5 V as the better negative working potential to ensure larger current response and smaller noise.

The electrocatalytic reduction behavior of $CoMn_2O_4$/GCE to 5 mM H_2O_2 in PBS solution with different pH values was studied under negative working potential of −0.5 V. As illustrated in Fig. 4B, as the pH value increases, the current response increases gradually and reaches the maximum at pH of 7.0. After that, the current response decreases when pH value is larger than 7.0. Thus, the better pH value during electrochemical test is determined as 7.0 (RSD < 3.9%). Furthermore, the amount of liquid containing the sample dropped onto the surface of bare GCE was also examined. As depicted in Fig. 4C, the amperometric response to H_2O_2 reaches the maximum at dropping amount of 10 μL. Afterwards, the amperometric response decreases with the dropping amount of 12 μL. Such results illustrate that the increased material thickness on GCE surface as the dropping amount increases hinders the rapid electron transfer and reduces the transfer efficiency. Thus, the best dropping amount is 10 μL (RSD < 3.2%). Based on the above experiments, the optimum conditions for testing the electrocatalytic H_2O_2 sensing performance of $CoMn_2O_4$/GCE are as below: negative working potential being −0.5 V, pH value of PBS being 7.0, and the dropping amount being 10 μL.

As shown in the CV curves (Fig. S4), no obvious redox peaks were detected between −0.5 and −0.4 V for bare GCE and different modified electrodes in PBS (pH = 7.0) without H_2O_2. In comparison, when 25 mM H_2O_2 was added to the above system, it can be seen from the CV curves in Fig. 5A that the modified electrodes have obvious reduction peaks around −0.5 V, indicating that they all have a certain electrocatalytic capacity for H_2O_2. The current responses gradually increase in the order of Mn_2O_3/GCE < Co_3O_4/GCE < $CoMn_2O_4$/GCE, which shows that the $CoMn_2O_4$/GCE has better electrocatalytic H_2O_2 sensing performance. This excellent catalytic performance originates from the synergism of large electrochemical effective area and small R_{ct}, as well as the unique $CoMn_2O_4$ hollow nanosphere structure and Co/Mn redox coupling.

Fig. 5B illustrates the CV curves of CoMn2O4/GCE to 25 mM H2O2 in PBS at different scan rates, and the inset is a partial enlarged view during the range of −0.6 to −0.4 V. One can see that the reduction peak current value gradually increases as the scan rate increases. During 0.24–0.40 V s-1, the reduction peak current (I_{pc}) value shows linearly increase to the square root of scan rate ($v^{1/2}$) with the linear regression equation being $I_{pc} = -189.30v^{1/2}$ -129.50 (R^2 = 0.998, Fig. 5C), indicating that the electrochemical reaction on the electrode surface is an irreversible process of diffusion control [30]. Simultaneously, as the scan rate increases, the reduction peak potential of $CoMn_2O_4$/GCE shifts to the negative value, and its reduction peak potential (E_{pc}) is linearly related to and logarithm scan rate (ln*v*) during 0.24–0.40 V s^{-1} (Fig. 5D). The linear regression equation is $E_{pc} = -0.029\ln v$ - 0.557 (R^2 = 0.996). Generally, for an irreversible electrochemical reaction process, the electron transfer coefficient (α) is 0.5 [32]. According to the Laviron's equation [32], the number of transferred electrons (n) in the diffusion process can be calculated to be 1.8 based on the linear slope of $-2.303RT/\alpha nF$, indicating that the electrocatalysis of modified $CoMn_2O_4$/GCE to H_2O_2 is a redox process with double electron transfer.

3.4. Amperometric detection of H_2O_2 on $CoMn_2O_4$/GCE

At −0.5 V, the electrocatalytic sensing performance of $CoMn_2O_4$/GCE was measured by adding different amounts of H_2O_2 to PBS

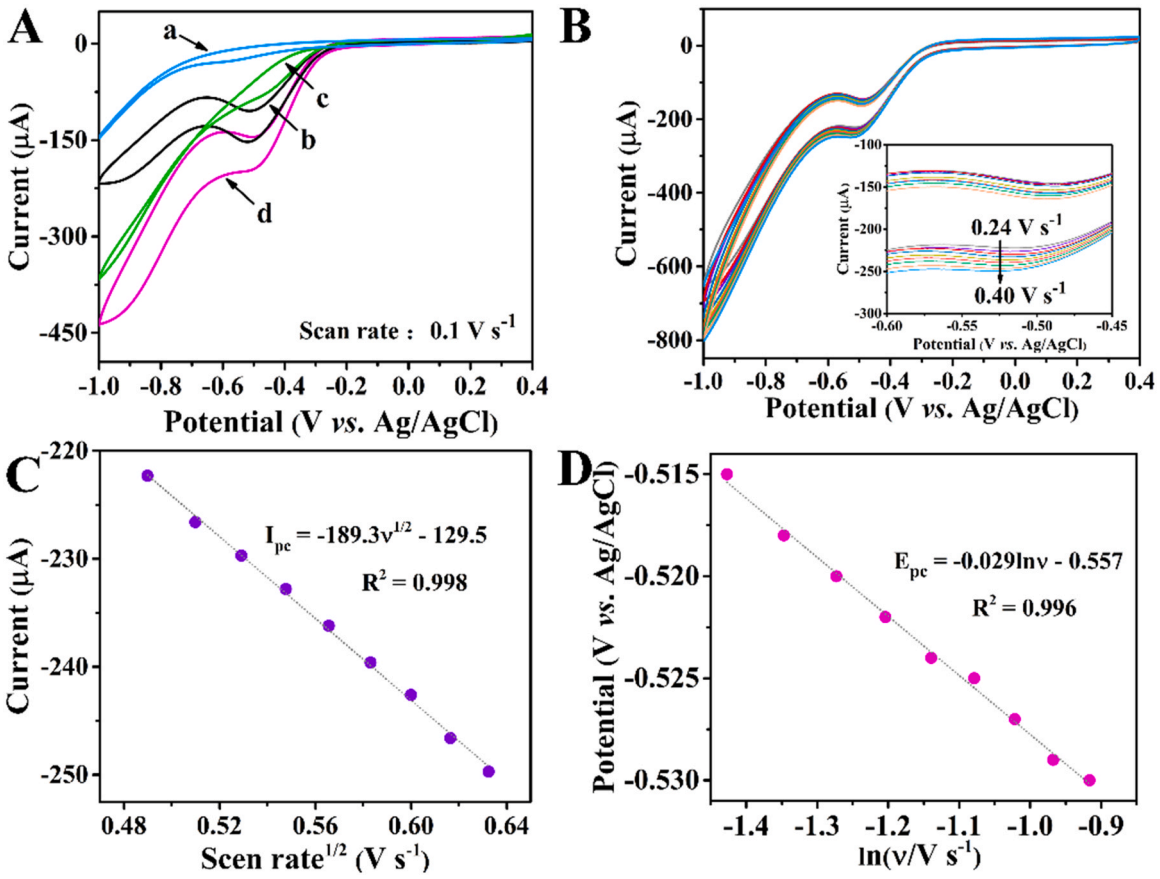

Fig. 5. (A) CV curves of different electrodes in the presence of 25 mM H_2O_2: GCE (a), Mn_2O_3/GCE (b), Co_3O_4/GCE (c), $CoMn_2O_4$/GCE (d); (B) CV curves of $CoMn_2O_4$/GCE to 25 mM H_2O_2 in 0.05 M PBS (pH = 7.0) at different scan rates (gradient of 0.02 V s^{-1}); (C) Plots of I_{pc} vs. square root of scan rate ($v^{1/2}$); (D) Plots of E_{pc} vs. the logarithm scan rate.

(0.05 M, pH = 7.0). As shown in Fig. 6A, the current response rapidly generates and gradually increases with the continuous injection of H_2O_2. And the current response of electrochemical sensor to H_2O_2 quickly reaches 95% balance within 5 s, thus confirming that $CoMn_2O_4$ hollow nanospheres have excellent electrocatalytic activity to H_2O_2. At the meantime, the current response is linearly related to the concentration of H_2O_2 (Fig. 6B) with equation being I_{pc}(μA) = 6.742 C(mM) - 1.009 (R^2 = 0.998, RSD = 4.02%). The electrochemical sensor exhibits high sensitivity of 28 μA mM^{-1} cm^{-2} and low detection limit of 0.38 μM (LOD = 3σ/S_d) to H_2O_2, which are obviously better than those of reported $CoMn_2O_4$/GCE [16]. Especially, its linear detection range (0.0012–100.4 mM) is the widest among reported spinel oxide-based electrochemical sensors (Table 1), which can avoid the complicated sample preparation process and shorten the period of electrochemical detection of H_2O_2, thereby facilitating portability and real-time operation in some practical applications.

In general, the adsorption of H_2O_2, breaking of O—O bond and generation of radical ·OH are important steps in the electrocatalytic H_2O_2 redox reaction. Hence, according to the above electrochemical results and related literature reports [38,39], the excellent electrocatalytic H_2O_2 sensing performance of porous $CoMn_2O_4$ hollow nanospheres may originate from the following reasons: (1) Compared with simple Mn_2O_3 and Co_3O_4 materials, the low-valence Co^{2+} and Mn^{2+} ions in $CoMn_2O_4$ spinel structure can promote the rapid capture and effective adsorption of H_2O_2 molecules on the surface of $CoMn_2O_4$ nanomaterial and form $Co^{2+} \overset{ads}{\leftarrow}$ OHHO $\overset{ads}{\rightarrow} Mn^{2+}$ transition state, which in turn increase the effective adsorption of H_2O_2 molecules on the surface of electrode; (2) Because transition metal ions with low-valence state have strong electron-donating ability, the electrons of Co^{2+} and Mn^{2+} ions can be quickly transferred to O atoms in H_2O_2. In this sense, the barrier potential of O—O bond fracture reduces, thus resulting in the rearrangement of O-O electrons and the rapid formation of ·OH radicals, accompanied by the oxidation of low-valence metal ions (Co^{3+}-·OHHO-Mn^{3+}); (3) The redox coupling of different valence metal ions can promote the rapid charge transfer and provide more electrocatalytic activity centers, which makes the H_2O_2 molecules can be quickly dissociated into $2OH^-$ ion ($H_2O_2+2e^- \rightarrow 2OH^-$). Then, the generated $2OH^-$ ion further combine with $2H^+$ protons to form water molecules ($2OH^-+2H^+ \rightarrow 2H_2O$). In addition, the excellent electrocatalytic H_2O_2 sensing performance is also related to the unique microstructure characteristics of $CoMn_2O_4$ nanomaterial. The hollow nanospheres constructed by small-size nanoparticles possess broad pore size distribution and large specific surface area, which can not only efficiently shorten diffusion path of electrons and analytes, promoting the charge transfer capacity and transfer efficiency, but also expose more electrochemical activity sites, ensuring high contact rate between target analytes and electrocatalyst. Especially, the internal hollow structure can accommodate more H_2O_2 molecules in the cavity to broaden the linear detection range of modified electrode, thus providing an efficient platform for electrochemical detection of H_2O_2. Hence, the excellent electrochemical sensing performance of $CoMn_2O_4$/GCE sensor to H_2O_2 is derived from the synergism of Co^{3+}/Co^{2+} and Mn^{3+}/Mn^{2+} redox couplings, as well as the inherent microstructure characteristics of hollow nanospheres.

3.5. The selectivity, stability and practicality of $CoMn_2O_4$/GCE

The selectivity, stability and reproducibility are important indicators for evaluating the practical application of electrochemical sensor. Generally, during the detection of H_2O_2 in biological samples,

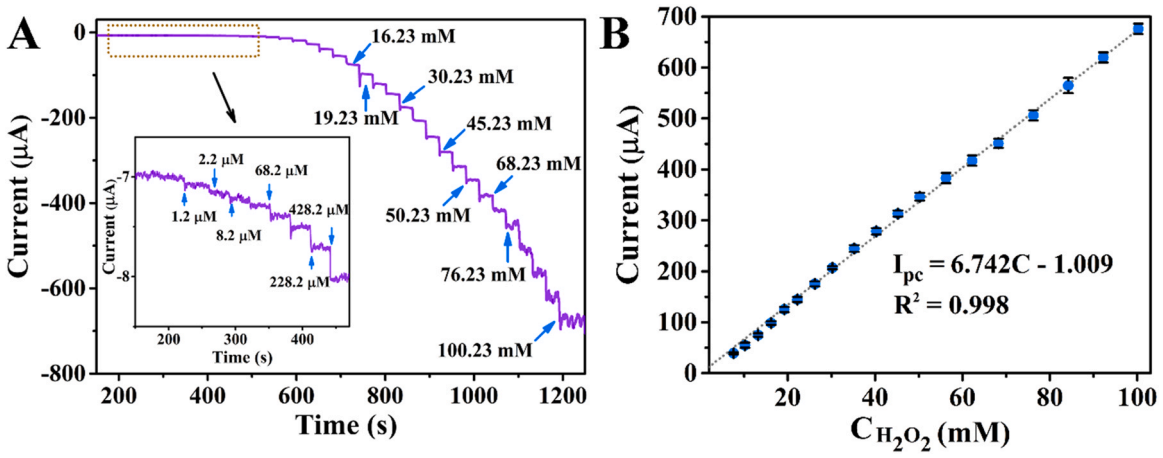

Fig. 6. (A) The *i-t* curve of $CoMn_2O_4$/GCE with continuous injection of H_2O_2 under negative working potential of −0.5 V (inset: enlargement *i-t* curve within 470 s); (B) The calibration plots of current response to concentration of H_2O_2.

Table 1
Comparison of $CoMn_2O_4$/GCE and reported electrochemical H_2O_2 sensors based on spinel oxides.

Electrochemical sensors	Electrolytes	Linear detection range (mM)	Detection limit (μM)	Refs.
$CoMn_2O_4$/GCE	**0.05 M PBS**	**0.0012–100.23**	**0.38**	**This work**
$CoMn_2O_4$/GE[a]	0.1 M PBS	1–1000	40.2	[16]
$ZnMn_2O_4$/GCE	0.2 M NaOH	0.02–15	0.13	[33]
$ZnMn_2O_4$/rGO/GCE[b]	0.2 M NaOH	0.0003–6	0.012	[34]
$ZnCr_2O_4$/CNTs/GCE[c]	0.1 M PBS	0.05–34.8	0.11	[35]
$ZnCrCoO_4$/NCNTs/GCE[d]	0.1 M PBS	0.001–7.33	1.0	[36]
$NiCo_2O_4$/GCE	0.1 M PBS	0.00026–6.6	0.009	[37]
$NiCo_2O_4$/GNC/GE[e]	0.1 M NaOH	0.02–0.7	1.7	[4]
$NiCo_2O_4$/$CoNiO_2$/rGO/GCE	0.1 M PBS	0.005–12	0.41	[38]
$CuCo_2O_4$/GCE	0.1 M NaOH	0.01–8.9	3.0	[3]
$CuCo_2O_4$/CeO_2/CNTs/GCE	0.1 M PBS	0.001–7.31	0.16	[39]
$CoFe_2O_4$/GCE	0.1 M KOH	0.005–17	0.5	[40]
$CoFe_2O_4$/SPCEs[f]	0.05 M PBS	–	2.59	[41]
$CoFe_2O_4$/CNTs/GCE	0.1 M PBS	0.005–0.05	0.05	[42]
$CoFe_2O_4$/CdSe/RIF/GCE[g]	0.1 M PBS	0.007–1.43	0.38	[43]
$MnFe_2O_4$/GCE	0.1 M PBS	0.001–24	0.3	[44]
$MnFe_2O_4$/SPCEs	0.05 M PBS	–	5.64	[41]
$MnFe_2O_4$/rGO/GCE	0.1 M PBS	0.001–22	0.35	[45]
$CuFe_2O_4$/PCF/GCE[h]	0.1 M NaOH	0.11–22.0	1.2	[46]
$CuFe_2O_4$/rGO/GCE	0.1 M PBS	0.001–11	0.35	[47]
$CuFe_2O_4$/rGO/CPE[i]	0.1 M PBS	0.002–0.2	0.52	[48]
$ZnFe_2O_4$/Pt/rGO/GCE	0.1 M PBS	0.0005–10.2	0.1	[49]

Note: a-GE: graphite electrode; b-rGO: reduced graphene oxide; c-CNTs: carbon nanotubes; d-NCTs: nitrogen-doped carbon nanotubes composite; e-GNC: graphene nanoclusters; f-SPCEs: screen-printed carbon electrodes; g-RIF: rifampicin; h-PCF: porous carbon nanowires; i-CPE: carbon paste electrode.

the common interfering substances in body fluids, for instance ascorbic acid (AA), dopamine (DA), epinephrine (E), glucose (Glu), uric acid (UA), L-cysteine (Lcy), glutamic acid (Gln), sodium nitrite ($NaNO_2$), sodium chloride (NaCl), etc., may interfere with the accurate detection of H_2O_2 by modified electrode. Fig. 7A shows the current-time curve of $CoMn_2O_4$/GCE to H_2O_2 in 0.05 M PBS (pH = 7.0) buffer with the successive addition of the above-mentioned interfering compounds (50 mM). The result shows that the presence of these interferents has almost no influence on the determination of H_2O_2 although their concentration is 10 times higher than that of

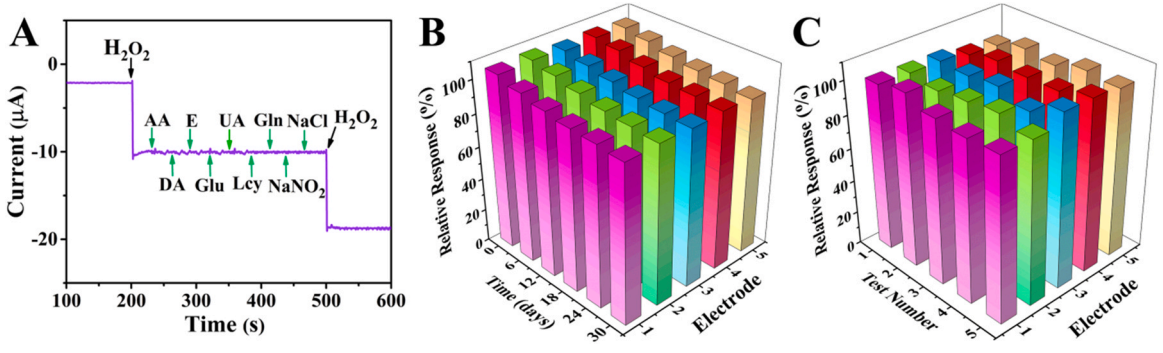

Fig. 7. (A) Current-time curve of $CoMn_2O_4$/GCE electrode with continuous addition of H_2O_2 at the presence of different interference substances; (B) Stability of 5 different $CoMn_2O_4$/GCE; (C) Reproducibility of 5 different electrodes to 5 mM H_2O_2.

Table 2
Determination of H_2O_2 in rat serum and commercial disinfectant samples using $CoMn_2O_4$/GCE sensor.

Samples	H_2O_2 added (mM)	H_2O_2 found (mM)	Recovery (%)	RSD (%)
Rat serum sample	0	–	–	–
1	5	4.88	97.60	2.08
2	10	9.65	96.50	3.24
3	15	14.83	98.87	2.17
Disinfectant	0	0.35	–	–
1	5	5.48	102.35	2.73
2	10	10.02	96.77	1.92
3	15	15.16	98.74	2.32

H_2O_2. When 5 mM H_2O_2 is added, obvious current response generates and quickly reaches stability, indicating that the $CoMn_2O_4$/GCE electrode has a good selectivity for the detection of H_2O_2 in PBS. The stability of five individual $CoMn_2O_4$/GCE is tested every six days with the addition of 5 mM H_2O_2 into the PBS solution over a 30-day period. As shown in Fig. 7B, although the current responses for the five electrodes are slightly reduced, it can still be maintained at 90% of the initial value with the relative standard deviation (RSD) during the range of 2.53–3.25%, indicating the good stability of fabricated $CoMn_2O_4$/GCE electrochemical sensors. In addition, reproducibility of the above five individual electrodes are investigated by adding 5 mM H_2O_2 into PBS buffer, and each electrode is successively measured for five times. The results in Fig. 7C show that the RSD of current signal for each electrode falls in the range of 1.96–3.08%. Meanwhile, the RSD for five different electrodes during the same test process is 1.02–3.32%. Both results illustrate the good reproducibility of the modified sensors. Therefore, the above electrochemical results show that the simply prepared $CoMn_2O_4$/GCE electrode exhibits satisfactory selectivity, stability and reproducibility.

To estimate the practical application ability of the $CoMn_2O_4$/GCE electrode, it was applied to detect H_2O_2 in rat serum sample and commercial disinfectant. The above-mentioned serum and disinfectant samples containing different H_2O_2 concentrations were measured by standard addition method. Each sample was measured in three parallel times with the obtained results being listed in Table 2. It can be seen that the recovery rate of serum sample is between 96.50% and 98.87% with the RSD falling in the range of 2.08–3.24%, while the recovery rate of disinfectant sample is between 96.77% and 102.35% with the RSD falling in the range of 1.92–2.73%. It should be pointed out that the present $CoMn_2O_4$/GCE electrochemical sensor has a better accurate recovery rate close to 100% and a smaller RSD rather than most reported electrochemical H_2O_2 sensors to various serums from different animals (Table S1). These results demonstrate that $CoMn_2O_4$/GCE has a satisfactory recovery rate for H_2O_2 in rat serum and commercial disinfectant, and further prove the good accuracy of the above-mentioned method. Therefore, the electrochemical sensor constructed from simply prepared $CoMn_2O_4$ hollow nanospheres has certain application potential in related environmental and biological fields.

4. Conclusions

In summary, $CoMn_2O_4$ hollow nanospheres with diameter of ~ 200 nm were facilely prepared by using PVP as structure directing agent, which assembled from small-size particles and has multi-level pore distribution. The enzyme-free electrochemical sensor obtained from simple drop-coating $CoMn_2O_4$ hollow nanospheres onto the surface of bare GCE presents better electrochemical H_2O_2 sensing performance, which mainly derives from the inherent microstructure characteristics of hollow nanospheres and the synergistic effect of Co^{3+}/Co^{2+} and Mn^{3+}/Mn^{2+} redox coupling. At optimum negative working potential of −0.5 V, the $CoMn_2O_4$/GCE sensor exhibits rapidly sensitive response and low detection limit of 0.38 μM to H_2O_2 in PBS buffer (pH = 7.0), good selectivity and stability. Especially, the linear detection range of 0.0012–100.4 mM is the widest among reported spinel oxide-based electrochemical sensors. Meanwhile, the $CoMn_2O_4$/GCE sensor shows good H_2O_2 recovery rate in rat serum and commercial disinfectant. Therefore, the electrochemical sensor constructed from simply prepared $CoMn_2O_4$ hollow nanospheres has potential practical application in related fields of environment, food and biology.

CRediT authorship contribution statement

Yuan Gao: Methodology, Investigation, Writing – original draft. **De-Rui Kong:** Methodology, Formal analysis. **Zhu-Yan Zhang:** Methodology, Formal analysis. **Xian-Fa Zhang:** Methodology, Formal analysis. **Zhao-Peng Deng:** Formal analysis, Investigation, Writing – review & editing. **Li-Hua Huo:** Methodology, Formal analysis. **Shan Gao:** Formal analysis, Investigation, Writing – review & editing.

Declaration of Competing Interest

The authors declare that they have no known competing financial interests or personal relationships that could have appeared to influence the work reported in this paper.

Acknowledgments

This work is financial supported by the International Science & Technology Cooperation Program of China [2016YFE0115100]; the Scientific and Technological Innovation Talents of Harbin [2016RAQXJ005]; and the Young Innovation Talents of College in Heilongjiang Province [UNPYSCT-2016074]. We thank the Key Laboratory of Functional Inorganic Material Chemistry, Ministry of Education, Heilongjiang University for supporting this study.

Appendix A. Supplementary material

Supplementary data associated with this article can be found in the online version at doi:10.1016/j.jallcom.2021.163158.

References

[1] S. Keerthana, A. Rajapriya, C. Viswanathan, N. Ponpandian, Enzyme like-colorimetric sensing of H_2O_2 based on intrinsic peroxidase mimic activity of WS_2 nanosheets anchored reduced graphene oxide, J. Alloy. Compd. 889 (2021) 161669, https://doi.org/10.1016/j.jallcom.2021.161669
[2] L. Li, B.Y. Li, H. Liu, M.Q. Li, B.H. Wang, Photoelectrochemical sensing of hydrogen peroxide using TiO_2 nanotube arrays decorated with RGO/CdS, J. Alloy. Compd. 815 (2020) 152241, https://doi.org/10.1016/j.jallcom.2019.152241
[3] D. Cheng, T. Wang, G.X. Zhang, H.M. Wu, H. Mei, A novel nonenzymatic electrochemical sensor based on double-shelled $CuCo_2O_4$ hollow microspheres for glucose and H_2O_2, J. Alloy. Compd. 819 (2020) 15304, https://doi.org/10.1016/j.jallcom.2019.153014
[4] B.S. Kumar, V.C. Gudla, R. Ambat, S.K. Kalpathy, S. Anandhan, Graphene nanoclusters embedded nickel cobaltite nanofibers as multifunctional electrocatalyst for glucose sensing and water-splitting applications, Ceram. Int. 45 (2019) 25078–25091, https://doi.org/10.1016/j.ceramint.2019.03.155
[5] S. Ramesh, K. Karuppasamy, D. Vikraman, P. Santhoshkumar, C. Bathula, R.R. Palem, A. Kathalingam, H.S. Kim, J.H. Kim, H.S. Kim, Sheet-like morphology $CuCo_2O_4$ bimetallic nanoparticles adorned on graphene oxide composites for symmetrical energy storage applications, J. Alloy. Compd. 892 (2021) 162182, https://doi.org/10.1016/j.jallcom.2021.162182
[6] D.X. Yin, X.Y. Cao, X.W. Liu, Z. Yang, Z.X. Liu, D.M. Wang, Q.Y. Liu, X.X. Zhang, X. Zhang, Rapid colorimetric sensing of ascorbic acid based on the excellent peroxidase-like activity of Pt deposited on $ZnCo_2O_4$ spheres, New J. Chem. 44 (2020) 12002, https://doi.org/10.1039/d0nj02795b
[7] Y. Gao, B. Li, Z. Zhang, X. Zhang, Z. Deng, L. Huo, S. Gao, $CuMn_2O_4$ spinel nanoflakes for amperometric detection of hydrogen peroxide, ACS Appl. Nano Mater. 4 (2021) 6832–6843, https://doi.org/10.1021/acsanm.1c00898
[8] W.X. Gu, C.Q. Li, J.H. Qiu, J.F. Yao, Facile preparation of porous hollow $Co_xMn_{3-x}O_4$ normal-reverse coexisted spinel for toluene oxidation, J. Alloy. Compd. 892 (2021) 162185, https://doi.org/10.1016/j.jallcom.2021.162185

[9] Q. Zhao, Z.H. Yan, C.C. Chen, J. Chen, Spinels: controlled preparation, oxygen reduction/evolution reaction application, and beyond, Chem. Rev. 117 (2017) 10121–10211, https://doi.org/10.1021/acs.chemrev.7b00051

[10] M. Dong, H.L. Hu, S.J. Ding, C.C. Wang, L. Li, A facile synthesis of $CoMn_2O_4$ nanosheets on reduced graphene oxide for non-enzymatic glucose sensing, Nanotechnology 32 (2021) 055501, https://doi.org/10.1088/1361-6528/abc112

[11] A. Muthumariappan, K. Sakthivel, S.M. Chen, T.W. Chen, A.M. Elgorban, M.S. Elshikh, N. Marraiki, Evaluating an effective electrocatalyst for the rapid determination of triptan drug (MaxalTM) from (mono and binary) transition metal (Co, Mn, CoMn, MnCo) oxides via electrochemical approaches, New J. Chem. 44 (2020) 605–613, https://doi.org/10.1039/c9nj04462k

[12] N. Bashir, M. Akhtar, H.Z.R. Nawaz, M.F. Warsi, I. Shakir, P.O. Agboola, S. Zulfiqar, A high performance electrochemical sensor for Pb^{2+} ions based on carbon nanotubes functionalized $CoMn_2O_4$ nanocomposite, ChemistrySelect 5 (2020) 7909–7918, https://doi.org/10.1002/slct.202001393

[13] R. Balaji, V. Renganathan, S.M. Chen, V. Singh, Selective and high-performance electrochemical sensor for cadmium ions based on intimate binary spinel $CoMn_2O_4$ nanostructures, ChemistrySelect 4 (2019) 13123–13130, https://doi.org/10.1002/slct.201902573

[14] J. Ma, W.H. Zhang, L. Zheng, Y.Y. Sun, R.Y. Jin, G.Z. Zhao, Y.Q. Liu, Direct formation of (Co, Mn)$_3O_4$ nanowires/Ni composite foam for electrochemical detection, J. Alloy. Compd. 663 (2016) 230–234, https://doi.org/10.1016/j.jallcom.2015.12.123

[15] Y. Wang, Z.G. Nie, X.Y. Li, Y. Zhao, H. Wang, Highly sensitive and selective electrochemical sensor based on porous graphitic carbon nitride/$CoMn_2O_4$ nanocomposite toward heavy metal ions, Sens. Actuators B Chem. 346 (2021) 130539, https://doi.org/10.1016/j.snb.2021.130539

[16] W.F. Liu, Z.H. Zhou, L. Yin, Y.M. Zhu, J. Zhao, B. Zhu, L.B. Zheng, Q. Jin, L. Wang, A novel self-powered bioelectrochemical sensor based on $CoMn_2O_4$ nanoparticle modified cathode for sensitive and rapid detection of hydrogen peroxide, Sens. Actuators B Chem. 271 (2018) 247–255, https://doi.org/10.1016/j.snb.2018.05.070

[17] J.Y. Sun, L.P. Xu, Z.X. Shi, Q.Q. Zhao, H.B. Wang, T. Gan, Morphology-tunable hollow Mn_2O_3 nanostructures: highly efficient electrocatalysts and their electrochemical sensing for phenolic endocrine disruptors via toughening of graphene oxide, Sens. Actuators B Chem. 327 (2021) 128889, https://doi.org/10.1016/j.snb.2020.128889

[18] M.Y. Wang, J.H. Zhong, Z.H. Zhu, A.M. Gao, F.Y. Yi, J.Z. Ling, J.N. Hao, D. Shu, Hollow NiCoP nanocubes derived from a Prussian blue analogue self-template for high-performance supercapacitors, J. Alloy. Compd. 893 (2021) 162344, https://doi.org/10.1016/j.jallcom.2021.162344

[19] Y.D. Cui, G.B. Yi, L.W. Liao, Synthesis and Application of Polyvinylpyrrolidone, Science Press, Beijing, 2001.

[20] Y.T. Zhang, S. Liu, Y. Li, D.M. Deng, X.J. Si, Y.P. Ding, H.B. He, L.Q. Luo, Z.X. Wang, Electrospun graphene decorated $MnCo_2O_4$ composite nanofibers for glucose biosensing, Biosens. Bioelectron. 66 (2015) 308–315, https://doi.org/10.1016/j.bios.2014.11.040

[21] K. Cheng, F. Yang, G.L. Wang, J.L. Yin, D.X. Cao, Facile synthesis of porous (Co, Mn)$_3O_4$ nanowires free-standing on a Ni foam and their catalytic performance for H_2O_2 electroreduction, J. Mater. Chem. A 1 (2013) 1669, https://doi.org/10.1039/c2ta00219a

[22] S.A. Hosseini, A. Niaei, D. Salari, S.R. Nabavi, Nanocrystalline AMn_2O_4 (A = Co, Ni, Cu) spinels for remediation of volatile organic compounds-synthesis, characterization and catalytic performance, Ceram. Int. 38 (2012), https://doi.org/10.1016/j.ceramint.2011.09.057 1655-166.

[23] K.N. Hui, K.S. Hui, Z.K. Tang, V.V. Jadhav, Q.X. Xia, Hierarchical chestnut-like $MnCo_2O_4$ nanoneedles grown on nickel foam as binder-free electrode for high energy density asymmetric supercapacitors, J. Power Sources 330 (2016) 195–203, https://doi.org/10.1016/j.jpowsour.2016.08.116

[24] N. Kanaujiya, N. Kumar, M. Singh, Y. Sharma, G.D. Varma, $CoMn_2O_4$ nanoparticles decorated on 2D MoS_2 frame: a synergetic energy storage composite material for practical supercapacitor applications, J. Energy Storage 35 (2021) 102302, https://doi.org/10.1016/j.est.2021.102302

[25] L.H. Liu, M. Yang, H. Zhao, Y.M. Xu, X.L. Cheng, X.F. Zhang, S. Gao, H.Y. Song, L.H. Huo, Co_3O_4/carbon hollow nanospheres for resistive monitoring of gaseous hydrogen sulfide and for nonenzymatic amperometric sensing of dissolved hydrogen peroxide, Microchim. Acta 186 (2019) 184, https://doi.org/10.1007/s00604-019-3253-8

[26] F.J. Ren, T. Wang, H.T. Liu, D.S. Liu, R. Zhong, C.Y. You, W.J. Zhang, S.Y. Lv, S.S. Liu, H. Zhu, L. Chang, B. Wang, $CoMn_2O_4$ nanoparticles embed in graphene oxide aerogel with three-dimensional network for practical application prospects of oxytetracycline degradation, Sep. Purif. Technol. 259 (2021) 118179, https://doi.org/10.1016/j.seppur.2020.118179

[27] X.F. Chen, L. Qie, L.L. Zhang, W.X. Zhang, Y.H. Huang, Self-templated synthesis of hollow porous submicron $ZnMn_2O_4$ sphere as anode for lithium-ion batteries, J. Alloy. Compd. 559 (2013) 5–10, https://doi.org/10.1016/j.jallcom.2013.01.036

[28] J. Xia, Q. Wang, M. Yang, H. Wu, Reliable electroanalysis of Hg (II) in water via flower-like porous $MnCo_2O_4$: excellent multilayer adsorption and (Mn, Co)(II)/(Mn, Co)(III) cycles, Sens. Actuators B Chem. 326 (2021) 129008, https://doi.org/10.1016/j.snb.2020.129008

[29] M. Asif, A. Aziz, G. Ashraf, Z.Y. Wang, J.L. Wang, M. Azeem, X.D. Chen, F. Xiao, H.F. Liu, Facet-inspired core-shell gold nanoislands on metal oxide octadecahedral heterostructures: high sensing performance toward sulfide in biotic fluids, ACS Appl. Mater. Interfaces 10 (2018) 36675–36685, https://doi.org/10.1021/acsami.8b12186

[30] J. Cheng, Y.F. Li, J. Zhong, Z.W. Lu, G.T. Wang, M.M. Sun, Y.Y. Jiang, P. Zou, X.X. Wang, Q.B. Zhao, Y.Y. Wang, H.B. Rao, Molecularly imprinted electrochemical sensor based on biomass carbon decorated with MOF-derived Cr_2O_3 and silver nanoparticles for selective and sensitive detection of nitrofurazone, Chem. Eng. J. 398 (2020) 125664, https://doi.org/10.1016/j.cej.2020.125664

[31] Y.Y. Dong, L. Zhang, Constructed 3D hierarchical porous wool-ball-like NiO-loaded AlOOH electrode materials for the determination of toxic metal ions, Electrochim. Acta 271 (2018) 27–34, https://doi.org/10.1016/j.electacta.2018.03.110

[32] J.J. Zhang, Q.W. Mei, Y.P. Ding, K. Guo, X.X. Yang, J.T. Zhao, Ordered mesoporous $NiCo_2O_4$ nanospheres as a novel electrocatalyst platform for 1–naphthol and 2–naphthol individual sensing application, ACS Appl. Mater. Interfaces 9 (2017) 29771–29781, https://doi.org/10.1021/acsami.7b08497

[33] Y.Y. Li, L. Tang, D.M. Deng, J.H. Ye, Z.Y. Wu, J.H. Wang, L.Q. Luo, A novel non-enzymatic H_2O_2 sensor using $ZnMn_2O_4$ microspheres modified glassy carbon electrode, Colloids Surf. B 179 (2019) 293–298, https://doi.org/10.1016/j.colsurfb.2019.04.008

[34] Y.Y. Li, K. Huan, D.M. Deng, L. Tang, J.H. Wang, L.Q. Luo, Facile synthesis of $ZnMn_2O_4$@rGO microspheres for ultrasensitive electrochemical detection of hydrogen peroxide from human breast cancer cells, ACS Appl. Mater. Interfaces 12 (2020) 3430–3437, https://doi.org/10.1021/acsami.9b19126

[35] Z. Shahnavaz, S.B.A. Hamid, Fabrication of a novel metal chromite — carbon nanotube composite for the highly efficient electrocatalytic reduction of hydrogen peroxide, Appl. Surf. Sci. 407 (2017) 379–385, https://doi.org/10.1016/j.apsusc.2017.01.254

[36] H.X. Wu, K. Xiao, T. Ouyang, Z. Wang, Y.B. Chen, N. Li, Z.Q. Liu, Co-Cr mixed spinel oxide nanodots anchored on nitrogen-doped carbon nanotubes as catalytic electrode for hydrogen peroxide sensing, J. Colloid Interface Sci. 585 (2021) 605–613, https://doi.org/10.1016/j.jcis.2020.10.040

[37] P. Balasubramanian, S.B. He, A. Jansirani, H.H. Deng, H.P. Peng, X.H. Xia, W. Chen, Oxygen vacancy confined nickel cobaltite nanostructures as an excellent interface for the enzyme-free electrochemical sensing of extracellular H_2O_2 secreted from live cells, New J. Chem. 44 (2020) 14050, https://doi.org/10.1039/d0nj03281f

[38] M.H. Wang, C.B. Wang, Y.K. Liu, B. Hu, L.H. He, Y.S. Ma, Z.H. Zhang, B.B. Cui, M. Du, Nonenzymatic amperometric sensor for hydrogen peroxide released from living cancer cells based on hierarchical $NiCo_2O_4$-$CoNiO_2$ hybrids embedded in partially reduced graphene oxide, Microchim. Acta 187 (2020) 436, https://doi.org/10.1007/s00604-020-04419-z

[39] J.W. Xie, D. Cheng, Z.L. Zhou, X. Pang, M.L. Liu, P. Yin, Y.Y. Zhang, H.T. Li, X.Y. Liu, S.Z. Yao, Hydrogen peroxide sensing in body fluids and tumor cells via in situ produced redox couples on two-dimensional holey $CuCo_2O_4$ nanosheets, Microchim. Acta 187 (2020) 469, https://doi.org/10.1007/s00604-020-04389-2

[40] M. Li, Y.P. Xiong, X.T. Liu, X.J. Bo, Y.F. Zhang, C. Han, L.P. Guo, Facile synthesis of electrospun MFe_2O_4 (M = Co, Ni, Cu, Mn) spinel nanofibers with excellent electrocatalytic properties for oxygen evolution and hydrogen peroxide reduction, Nanoscale 7 (2015) 8920, https://doi.org/10.1039/c4nr07243j

[41] X. Zhu, H.L. Zhao, X.H. Niu, T.T. Liu, L.B. Shi, M.B. Lan, A comparative study of carbon nanotube supported MFe_2O_4 spinels (M=Fe, Co, Mn) for amperometric determination of H_2O_2 at neutral pH values, Microchim. Acta 183 (2016) 2431–2439, https://doi.org/10.1007/s00604-016-1887-3

[42] S. Sahoo, P.K. Sahoo, S. Manna, A.K. Satpati, A novel low cost nonenzymatic hydrogen peroxide sensor based on $CoFe_2O_4$/CNTs nanocomposite modified electrode, J. Electroanal. Chem. 876 (2020) 114504, https://doi.org/10.1016/j.jelechem.2020.114504

[43] F. Mollarasouli, S. Kurbanoglu, K. Asadpour-Zeynali, S.A. Ozkan, Non-enzymatic monitoring of hydrogen peroxide using novel nanosensor based on $CoFe_2O_4$@CdSeQD magnetic nanocomposite and rifampicin mediator, Anal. Bioanal. Chem. 412 (2020) 5053–5065, https://doi.org/10.1007/s00216-019-02306-y

[44] K.W. Wang, W.J. Shen, Metal-organic framework-derived manganese ferrite nanocubes for efficient hydrogen peroxide sensing, Mater. Lett. 277 (2020) 128284, https://doi.org/10.1016/j.matlet.2020.128284

[45] G.P.J. Rani, J. Saravanan, S. Sheet, M.A.J. Rajan, Y.S. Lee, A. Balasubramani, G. Gnana kumar, The sensitive and selective enzyme-free electrochemical H_2O_2 sensor based on rGO/$MnFe_2O_4$ nanocomposite, Electrocatalysis 9 (2018) 102–112, https://doi.org/10.1007/s12678-017-0418-2

[46] M. Li, M.J. Lu, J.R. Yang, J. Xiao, L.N. Han, Y.J. Zhang, X.J. Bo, Facile design of ultrafine $CuFe_2O_4$ nanocrystallines coupled porous carbon nanowires: highly effective electrocatalysts for hydrogen peroxide reduction and the oxygen evolution reaction, J. Alloy. Compd. 809 (2019) 151766, https://doi.org/10.1016/j.jallcom.2019.151766

[47] C. Karthikeyan, K. Ramachandran, S. Sheet, D.J. Yoo, Y.S. Lee, Y. Satish Kumar, A.R. Kim, G. Gnana Kumar, Pigeon-excreta-mediated synthesis of reduced graphene oxide (rGO)/$CuFe_2O_4$ nanocomposite and its catalytic activity toward sensitive and selective hydrogen peroxide detection, ACS Sustain. Chem. Eng. 5 (2017) 4897–4905, https://doi.org/10.1021/acssuschemeng.7b00314

[48] A. Benvidi, M.T. Nafar, S. Jahanbani, M.D. Tezerjani, M. Rezaeinasab, S. Dalirnasab, Developing an electrochemical sensor based on a carbon paste electrode modified with nano-composite of reduced graphene oxide and $CuFe_2O_4$ nanoparticles for determination of hydrogen peroxide, Mater. Sci. Eng. C 75 (2017) 1435–1447, https://doi.org/10.1016/j.msec.2017.03.062

[49] L.Y. Ning, X.L. Guan, J.W. Ma, M. Wang, X.B. Fan, G.L. Zhang, F.B. Zhang, W.C. Peng, Y. Li, A highly sensitive nonenzymatic H_2O_2 sensor based on platinum, $ZnFe_2O_4$ functionalized reduced graphene oxide, J. Alloy. Compd. 738 (2018) 317–322, https://doi.org/10.1016/j.jallcom.2017.12.161